VU Research Portal

Integrated-optics Solutions for Biomedical Optical Imaging
Akca, Imran

published in
Advances in Optics: Reviews
2018

Link to publication in VU Research Portal

Chapter 9
Integrated-Optics Solutions for Biomedical Optical Imaging

B. Imran Akca

9.1. Introduction

Several novel optical imaging techniques have been developed over the past years to be used in basic biological research and clinical applications. Flourescence, confocal, Raman, and Brillioun microscopy are just a few of these optical techniques that are actively investigated by many research groups. Optical coherence tomography (OCT) is also one of these hot research areas which is a non-invasive, three-dimensional imaging technique that offers close-to-histology-level image quality [1]. Based on broadband spectral interferometry, OCT has enabled clinical applications ranging from ophthalmology to cardiology that revolutionized in vivo medical diagnostics. There are currently two distinct OCT technologies commercially available: time domain (TD) and Fourier domain (FD) OCT technology. Integrated optics offers unique solutions for OCT systems. Integrating several complex optical devices as miniaturized components on a single microchip improves mechanical stability for maintenance-free operation and accesses lithographic high-volume fabrication for dramatic cost reduction and improved repeatability. Miniaturized OCT systems have recently garnered attention for mainly their high potential in overcoming the size and cost problems of the bulky OCT systems [2, 3]. One major advantage of integrated optics is that the operation of the existing optical components can be reconfigured by controlling the material properties using temperature, voltage, or pressure. Despite this unique feature, OCT based upon integrated optical components has as yet not utilized it properly.

In this chapter, by exploiting the unique features of integrated optics, the design of a novel multiple-reference TD-OCT system, an akinetic beam scanner, and high-speed spectrometers with ultra-high resolution or broad bandwidth are presented. The TD-OCT system and the akinematic beam scanner are designed to work at 1300 nm wavelength

B. Imran Akca
Institute for Lasers, Life and Biophotonics Amsterdam, Department of Physics and Astronomy, VU University Amsterdam, Amsterdam, The Netherlands

range whereas spectrometers are designed for 800 nm range. In conventional TD-OCT systems depth scanning is achieved by modifying the relative optical path length difference of the reference and the sample arms in a sequential way using mechanical scanners. Due to the speed limitations and accompanying significant sensitivity decrease, and motion artifacts conventional TD-OCT systems fall behind FD-OCT systems in many applications. Formation of 2D images in many imaging techniques requires precise lateral scanning of the incident light beam using mechanical scanners such as galvanometer actuated mirrors. These mechanical scanners cause some major problems such as image distortion, phase errors, beam jitter, and inaccuracies due to non-uniform scan pattern, etc. Spectrometers are the core of many optical imaging modalities, such as Brillioun microscopy, SD-OCT, Raman microscopy etc. Having high speed, broad bandwidth, high resolution, and small footprint are the main requirements of a spectrometer.

The designs that are discussed in this chapter are all comprised of electro-optic switches and very compact delay lines. Firstly, the electro-optic switch design for the devices working at 1300 nm wavelength range will be discussed and later on the details of each device design will be given. Spectrometers that are designed at 800 nm wavelength range will be discussed separately in the following section.

9.2. Designs at 1300 nm

9.2.1. Material System

The proposed sample arm configuration was simulated for the lithium niobate (LN)-on-silicon waveguide platform as it is being one of the most versatile and well-developed active optical materials [4]. The material system is 300-nm-thick ion-sliced lithium niobate film on oxidized silicon wafer. The oxide thickness is 3 μm. The refractive index of the LN layer is 2.22 at 1300 nm, and its electro-optic (EO) coefficient is ($r_{33} \sim 30$ pm/V) [4]. Single mode rib waveguides with 0.2 μm of slab height and 1 μm of waveguide width were designed. The effective refractive index of the rib waveguide was calculated to be 1.85 by using beam propagation method (BPM) simulations. The three-dimensional illustration of the waveguide structure as well as the optical mode profile are given in Fig. 9.1. The minimum bending radius of the curved waveguides was calculated to be $R = 100$ μm with a bending loss of 0.01 dB/cm. The propagation loss of the LN waveguides defined by the ion-implantation-assisted wet etching is around 0.23 dB/cm. Metallic electrodes can be defined using gold or chromium. A *500-nm-thick silicon dioxide (SiO$_2$)* top cladding will be used to prevent propagation losses induced by the *electrodes.* The fiber-to-chip coupling losses (~6 dB) can be reduced to < 0.5 dB by using a high numerical aperture fiber [5].

9.2.2. Working Principle of the Electro-Optic Switch

One of the main components of the proposed designs is an electro-optic switch which is a wavelength-insensitive Mach-Zehnder-type interferometric coupler as illustrated in Fig. 9.2 [6, 7].
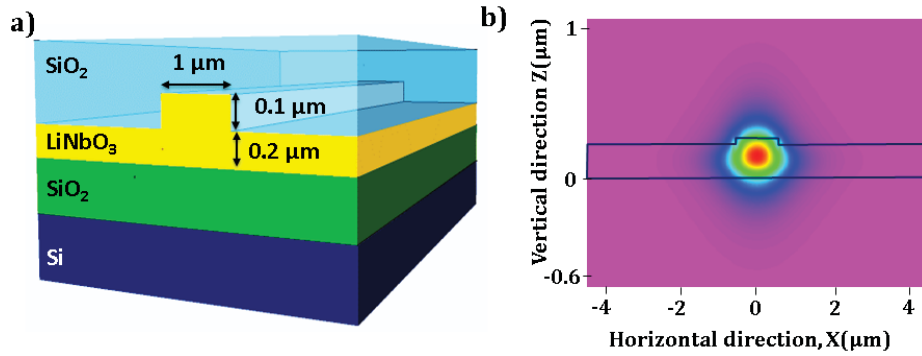
Fig. 9.1. (a) Three-dimensional view of the waveguide stack with relevant design parameters; (b) Beam propagation method simulation of the optical mode. The blue outline shows the cross-sectional profile of the waveguide geometry.
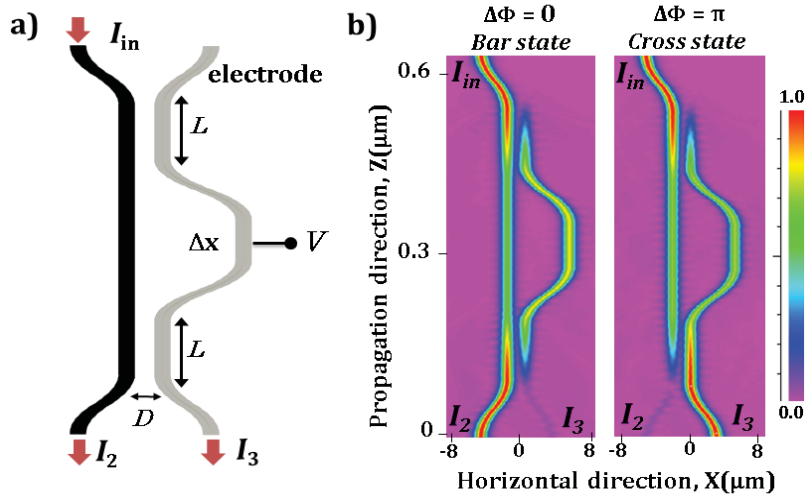

Fig. 9.2. (a) The schematic of the wavelength-insensitive electro-optic switch. An electrode is placed on top of the right arm of the coupler which is drawn in gray; (b) Beam propagation method simulation of the switch; (Left) No phase difference between coupler arms, the input light will stay in the same arm (bar state). (Right) For a π phase difference between coupler arms, the input light will cross-couple to the other arm (cross state). L, D, Δx are the lengths of the straight sections of the directional couplers, and the delay section, and the separation between coupler arms, respectively.

It is comprised of a pair of directional couplers connected by a delay section in which a phase shift is introduced. The second directional coupler cancels deviations introduced by the former, if these deviations are similar in both couplers. An electrode is placed on the right arm of the electro-optic switch as shown in gray in Fig. 9.2 (a). When the voltage is off, the lights on both arms will be in phase and the input light will stay in the same arm, i.e. bar state as illustrated in the left part of Fig. 9.2 (b). With the applied voltage, the effective refractive index of that arm is locally increased due to the electro-optic effect

which induces a phase difference between two arms. At a certain voltage value corresponding to a π phase difference between arms, the sample beam cross-couples to the other arm, i.e. cross state (Fig. 9.2 (c) right part). It is also possible to achieve switching operation using pressure-induced refractive index change by choosing the material technology accordingly.

9.2.3. Akinetic Beam Scanner Layout and Its Working Principle

The akinetic scanner design is comprised of two main components; namely electro-optic switches and two-mode interference based beam splitters/combiners. Fig. 9.3 (a) shows the akinetic scanner layout implemented in an integrated-OCT system centered at 1300 nm. For simplicity, only 4 arms of the scanner are shown in the figure. Input light is divided into two arms with an integrated 3 dB beam splitter; half of it towards the reference arm which is integrated on the same chip for further size reduction, the other half towards the sample arms. Each sample arm consists of an electro-optic switch (Fig. 9.3 (b)) for beam steering and a beam splitter/combiner (Fig. 9.3 (c)). The electro-optic switch changes the propagation direction of the sample beam from bar state to cross state by an applied voltage corresponding to π phase difference between coupler arms. By activating each switch sequentially, the sample beam can be steered from one imaging location to the next until whole imaging range is scanned.
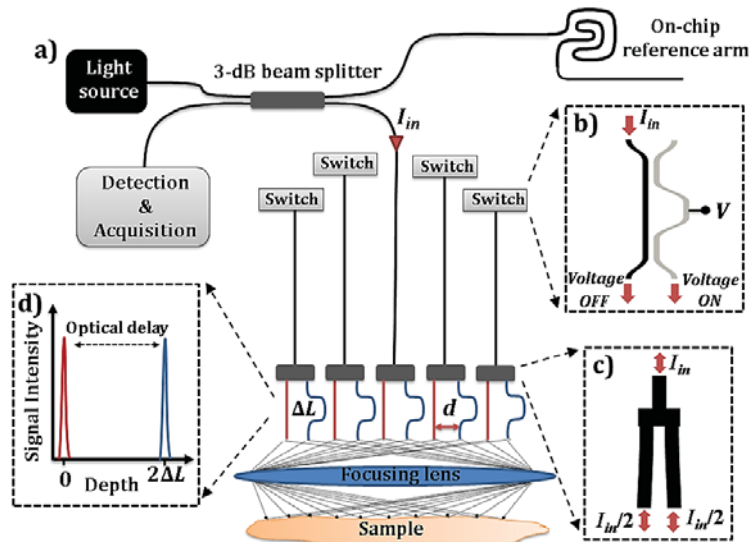

Fig. 9.3. (a) Akinetic beam scanner implemented in an integrated-OCT system. Light coming from the input waveguide is divided into two; half towards on-chip reference arm, half towards the sample arm where several electro-optic switches are placed. The end of each sample arm is divided into two branches with a constant length difference, i.e. ΔL, between each for simultaneous imaging; (b) Schematic of the electro-optic switch; (c) Schematic of the two-mode interference based beam splitter/combiner. The splitting ratio is 50/50; (d) Due to ΔL, signals from two different physical locations on the sample will be detected at two different depth locations which are separated by $2\Delta L$.

In order to double the imaging speed, each sample arm is divided into two branches with a certain length difference, i.e. ΔL, between them. In this way, two physical locations on the sample can be simultaneously illuminated. When images are formed, signals from two different locations will be detected at two different depths separated by $2\Delta L$ as depicted in Fig. 9.3 (d). The number of branches can be increased further in accordance with the desired speed improvement. The separation between each branch is chosen to be $d = 20$ µm. For a scanning range of 1 mm, 24 electro-optic switches are used which results in a scanner size of around 1 mm × 9 mm (9 mm²). Using the central part of a focusing lens, light can be successfully delivered into the tissue and collected back through same path. Returned signal from different sample locations are combined at the 3 dB coupler and interfered with light from the reference arm. A single detector and a high-speed data acquisition card is utilized to record interference signal from all beams simultaneously.

The switching time of an electro-optic coupler is only few nanoseconds, (<10 ns), therefore scanning of a 1 mm wide area on the sample would take approximately 200 nanoseconds. However, in order to avoid data acquisition related problems and increase the integration time for higher signal to noise ratio, it is necessary to apply some time delay between each imaging point. Even for a long time delay, e.g. 1 millisecond, a reasonably high scanning speed, i.e. ~1 kHz, can be achieved.

9.2.4. Multiple-Reference TD-OCT Layout and Its Working Principle

Fig. 9.4 is the schematic of the integrated-optics-based multiple-reference TD-OCT system in which the micro-chip is outlined by the red dashed-rectangle. For ease of understanding the first two levels of the light tapping mechanism are demonstrated. Here, a central wavelength of 1300 nm, an axial resolution of 20 µm, and a depth range of 1 mm are aimed at. Light coming from a broadband light source will be divided into two arms with a 3 dB coupler; half towards the sample, half towards the reference arm. There will be several electro-optically-controlled directional couplers placed on both sample and reference arms at certain distances. Imaging of different depths will be controlled by the additional length increment between consecutive reference beams (i.e. *a* in Fig. 9.4). According to *the Nyquist* sampling *theorem* the step size of the beam scanning should not be more than half of the axial resolution, i.e. 10 µm, which defines the length difference between consecutive reference points. Consequently, *a is* calculated to be 14 µm for this design by reckoning in the round trip of the light inside the tissue as well as the effective refractive indices of tissue and waveguides (n_e (tissue) × 10 µm × 2 = n_e (waveguide) × a, where n_e (tissue) = 1.4, n_e (waveguide) = 2.01)). For larger bandwidths, the group refractive indices of the waveguide and tissue have to be used for calculating *a*. There is no restraint on the additional length between tapping sections, i.e. *d,* however smaller *d* is favorable for compact devices.

9.2.5. Design Parameters of the Electro-Optic Switch

The design of the electro-optic switch was made in two steps. Firstly, lengths of the straight coupling sections of the directional coupler and the delay part were calculated to

achieve full coupling using equations given in [7] as $L = 95$ µm and $\Delta x = 0.28$ µm, respectively. The separation between coupler arms was chosen as $D = 1$ µm in order to reduce the overall device length to 0.65 mm. Secondly, the coupler designed in the first step was used to simulate the required mode effective refractive index increment for a π phase difference by scanning the refractive index difference (Δn) between coupler arms from 0 to 5×10^{-3} with 10^{-4} step size (Fig. 9.5 (a)). It was found to be $\Delta n = 2 \times 10^{-3}$. The required voltage value to induce such index difference was calculated to be 21 Volts by using below equation [8]

$$\Delta n(V) = \frac{1}{2} n_e^3 r_{33} \frac{V}{t} \Gamma,$$
(9.1)

for an overlap factor of $\Gamma = 0.3$, electro-optically active layer thickness of $t = 0.3$ µm, effective refractive index of $n_e = 1.85$, and electro-optic coefficient of $r_{33} = 30$ pm/V. The coupling loss was simulated to be 0.04 dB. The simulated splitting ratio between two arms stays constant over 100 nm bandwidth, as shown in Fig. 9.5(b). The coupling ratio remains the same even after a certain voltage applied on one arm of the coupler (Fig. 9.5 (b), bottom).
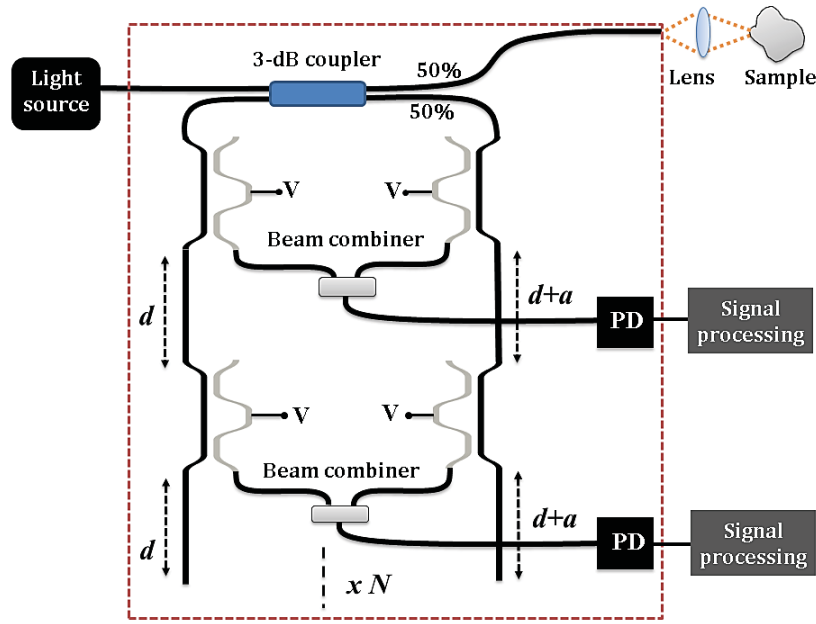

Fig. 9.4. Schematic of the proposed multiple-reference arm TD-OCT system based on integrated optics. Electro-optically-controlled directional couplers act as optical switches, which keep it on the same arm when there is no voltage, and cross-couple the light when there is a π phase difference due to electro-optic effect. The cross-coupled light from reference and sample arms will be combined at the beam combiner and sent to a photodetector (PD). Imaging of different depths will be controlled by the additional length increment between consecutive reference beams, i.e. a. The micro-chip is outlined by the red dashed-rectangle.
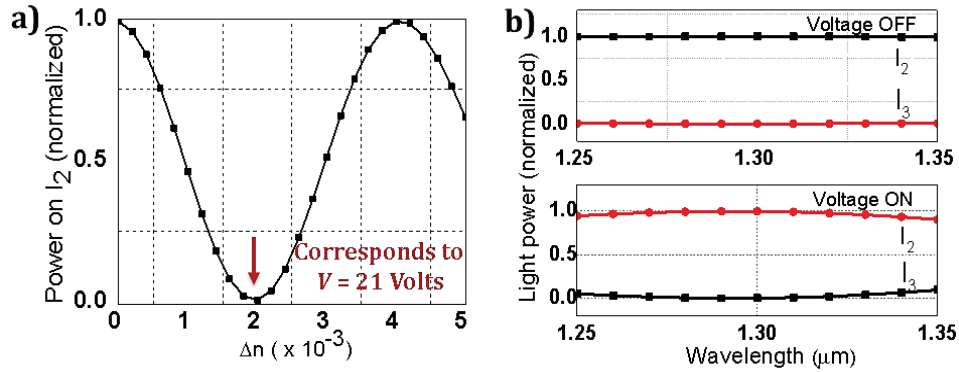
Fig. 9.5. Simulation results of the electro-optic switch (a) Refractive index difference between coupler arms versus power on the same arm (I_2). For $\Delta n = 2 \times 10^{-3}$, 99 % of the input light is cross-coupled to the other arm; (b) The coupler is wavelength independent for a wavelength range of 100 nm, and its wavelength independency does not change after the voltage is turned on.

The change in coupling ratio of the electro-optic switch due to the process non-uniformity and limitations in reproducibility has been investigated. The refractive index of the cladding layer can have non-uniformities of up to $\pm 3 \times 10^{-4}$, and the core layer can show thickness variations up to ± 1 % over the wafer. The waveguide width can vary by ± 0.1 μm. The simulation results of the effects of these process-dependent deviations are summarized in Table 9.1. The wavelength-independent couplers used in electro-switches are relatively fabrication tolerant devices as indicated in Table 9.1. Variations in the refractive index of the cladding layer has the minimum effect on coupling ratio whereas the maximum variation in coupling ratio was calculated to be 0.2 % for ± 1 % change in core thickness which is still insignificant.

Table 9.1. The Effect of the Technological Tolerances on Electro-optic Switch Performance.

Parameters		Effective index change (×10^{-3})	Coupling ratio change (%)
$\Delta w = \pm 0.1$ μm	w = 1.1 μm	5.5	0.09
	w = 0.9 μm	-6.5	-0.1
$\delta d_{core} = \pm 1$ %	d_{core} = 303 nm	2.6	0.2
	d_{core} = 297 nm	-2.6	-0.2
$\Delta n_{cladding} = \pm 3 \times 10^{-4}$	$n_{cladding}$ = 1.4488	0.2	0.01
	$n_{cladding}$ = 1.4482	-0.1	-0.009

9.2.6. Two-Mode Interference Beam Splitter/Combiner Design

The beam splitter/combiner used in the end of each arm of the TD-OCT system as well as in the akinetic scanner is based on two-mode interference (TMI). It is wavelength independent and compared to an optical Y junction it is more fabrication tolerant, and

reproducible. Fig. 9.6 (b) and Fig. 9.6 (c) demonstrate the beam propagation simulation results of the TMI-based beam splitter and combiner, respectively. The separation between input waveguides, the width and the length of the slab region are h = 0.8 μm, w = 3 μm, and l = 9 μm, respectively. The splitting ratio is constant over 200 nm wavelength range as shown in Fig. 9.6 (d). The overall loss of the beam combiner/splitter was simulated to be 0.18 dB.
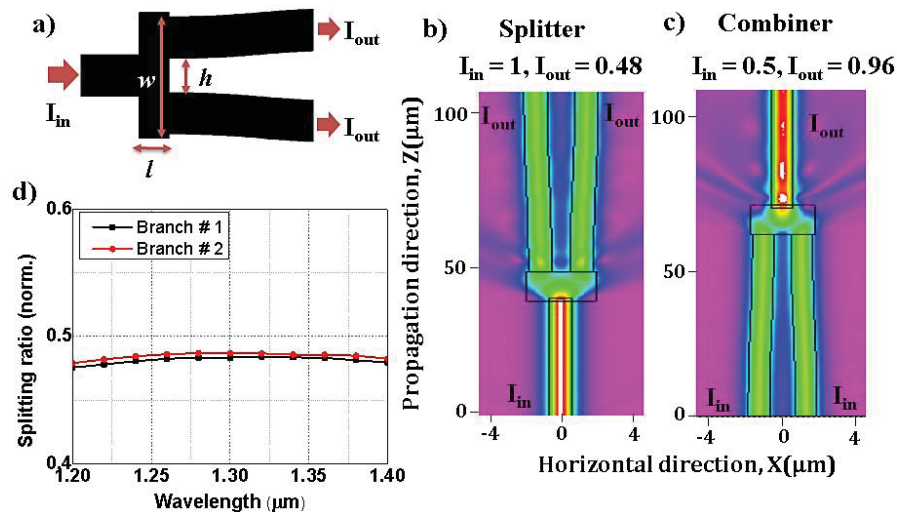

Fig. 9.6. (a) Schematic of the TMI-based beam splitter (b), and combiner (c). The loss of the splitter and combiner was simulated to be 0.18 dB. (d) The splitting ratio remains constant over 200 nm bandwidth range.

9.3. High-Speed Spectrometer Designs

Optical spectroscopy is an essential tool in numerous areas including biochemical sensing, material analysis, optical communication, and medical applications [9]. The development of a high-resolution on-chip spectrometer could enable compact, low-cost spectroscopy for portable sensing and increase lab-on-a-chip functionality. Motivated by this demand, several integrated microspectrometers have been realized in different configurations [10-13]. Most of these spectrometers rely on dispersive components which are inevitably bulky because their spectral resolution scales inversely with optical path length. Fourier transform spectroscopy (FTS) is a technique that uses interference of light rather than dispersion to measure the spectrum of a sample [14]. It is basically a Michelson interferometer with a movable mirror. The basis of this technique is the Fourier-pair relationship between the interferogram of a sample and its spectrum. The primary advantages of FTS compared to dispersive spectrometers are high optical throughput thereby greater signal-to-noise ratio, compact size, and relatively easily attainable high resolution which is constant over the entire spectral region as determined by the mirror displacement from the origin.

Although FTS can be more compact in size, its scanning interferometric configuration makes it slow for some applications where speed is a critical constraint [15]. Spatial heterodyne spectroscopy (SHS) is an interferometric Fourier-transform (FT) technique based on a modified Michelson interferometer with no moving parts and relying on analysis of stationary interference patterns [16]. The SHS concept was successfully implemented in bulk optics so far, and recently it has been proposed for planar waveguide implementation by Cheben et al. as a Fourier-transform arrayed waveguide grating (FT-AWG) microspectrometer [12]. Florjańczyk et al., have generalized the waveguide SHS FT concept into a waveguide Mach-Zehnder interferometer (MZI) array which was based on an array of independent MZIs with different phase delays [17]. Even though it is a promising technique, it is still challenging to place long delay lines on a single wafer to achieve ultrahigh resolution. As a follow-up, they have presented a spiral-based SHS FT design with a spectral resolution of 40 pm, and footprint of 12 mm^2 [18]. However, besides being quite lossy, the spectrometer size will still be significant if ultrahigh resolution is aimed at.

In this section, two novel FT spectrometer layouts are introduced; one with an ultrahigh-resolution of 500 MHz (~ 1 pm) in a very small footprint of 1 cm^2 and other one with larger bandwidth (40 nm). The ultrahigh-resolution spectrometer design is comprised of N = 60 MZIs whereas large-bandwidth spectrometer has N = 80 MZIs that are sequentially activated by voltage-controlled directional couplers. Compared to spiral-based FT spectrometer described in [18], the ultrahigh-resolution spectrometer layout will provide much smaller size for the same resolution in addition its N times larger throughput. The long optical delay between MZI arms is introduced by sequentially tapping the propagating light out at several locations on the light path which makes the overall device size very compact. The tapping operation is provided by electro-optically-controlled directional couplers that are placed on both interferometer arms with a certain length difference between consecutive tapping locations. Lithium niobate (LN)-on-silicon material technology was chosen for these specific designs, however it can be applied to other electro-optic materials. The proposed designs can be easily adjusted to realize spectrometers with different bandwidth and resolution combinations.

The electro-optic switch and the waveguide geometry were redesigned in accordance with the new wavelength range, i.e. 800 nm. Since the bandwidth range of the spectrometers is not more than 40 nm, directional couplers are preferred in electro-optic switch design in contrary to 1300-nm designs as it has a shorter length which reduces the device size significantly.

9.3.1. Material System at 800 nm

The proposed spectrometer ideas are simulated for the LN-on-silicon waveguide platform. The material system is 250-nm-thick ion-sliced lithium niobate film on oxidized silicon wafer. The oxide thickness is 3 μm. The refractive index of the LN layer is 2.25 at 800 nm. Single mode rib waveguides with 0.2 μm of slab height and 0.9 μm of waveguide width were designed. Fig. 9.7(b) demonstrates the cross-sectional beam profile of the mode obtained by using beam propagation method (BPM). The minimum bending radius

of the curved waveguides was calculated to be $R = 150$ μm with a bending loss of -0.005 dB/cm. A *500-nm-thick silicon dioxide (SiO₂)* top cladding will be used to prevent propagation losses induced by the *electrodes.* The simulated beam profile and the relevant waveguide parameters are given in Fig. 9.7 (b).

9.3.2. Electro-Optic Switch Design at 800 nm

Directional couplers used in both layouts were designed to act as voltage-controlled electro-optic switches with nanosecond switch time. A metallic electrode was placed on top of one of the straight waveguides of the directional coupler as shown in Fig. 9.7 (a).
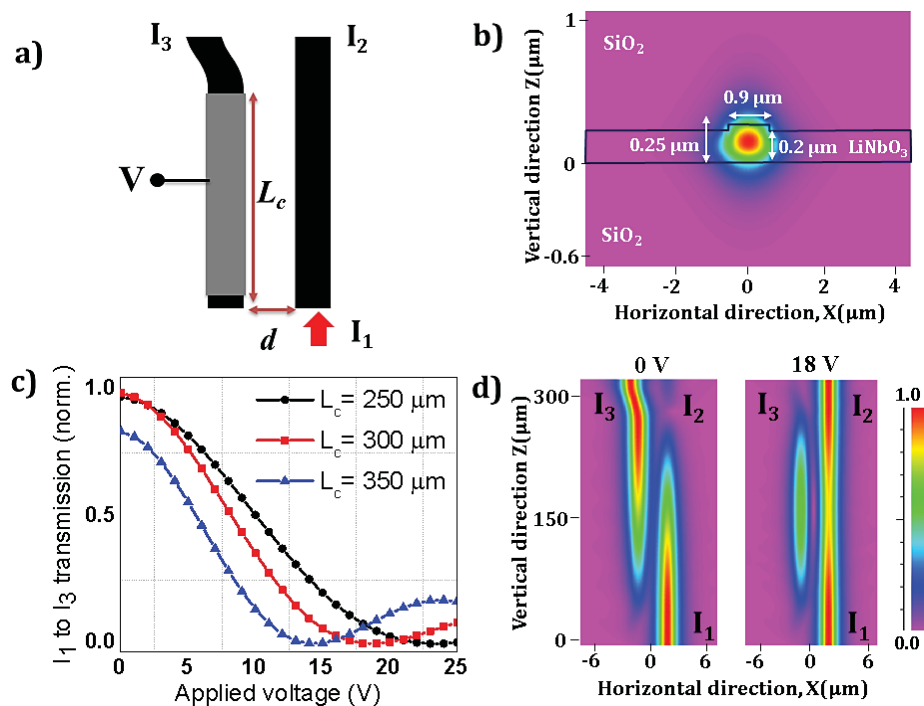

Fig. 9.7. (a) The schematic of the electro-optically-controlled integrated- optics-based directional coupler. Here I_1 is the input light, I_2 is the transmitted light, I_3 is the cross-coupled light, L_c is the electrode length, and d is the separation between coupler arms. (b) Beam propagation method simulation of the optical mode. The blue outline shows the cross-sectional profile of the waveguide geometry. Relevant waveguide parameters are given. (c) The amount of cross-coupling of the input light at different voltage values for different electrode lengths. The most optimum combination was obtained for an electrode length of 300 μm and an applied voltage value of V = 18 Volts. (d), right Voltage is OFF, the light will be cross-coupled to the other channel. (d), left Voltage is ON, V = 18 Volts, a π phase difference will be generated between coupler arms and the input light will stay in the same arm.

When there is no voltage on the electrodes, the lights on both arms will be in phase and the incoming light will be cross-coupled to the other arm. (Fig. 9.7 (d) left side). At a

certain voltage value (i.e. V = 18 Volts for this design), a π phase difference is generated between coupler arms which avoids cross-coupling of the light and forwards it to the next stage where a different spectral information is obtained (Fig. 9.7 (d) right side). This operation will be performed in a sequential order by switching the directional couplers on and off until all range is scanned. It is assumed that the coupling ratios at each directional coupler does not vary substantially across the entire bandwidth which is relatively small for the example considered here (i.e. 15 GHz). However, the non-uniformity of light coupling among individual directional couplers can be calibrated out as described in [17].The effective refractive index of the waveguide stack was calculated to be 2.0 for TE polarization. The expected change in the mode effective refractive index due to applied voltage (Δn (V)) was calculated to be $12 \times 10^{-5} \times V$ using Eq. (9.1) for an overlap factor of $\Gamma = 0.25$, electro-optically active layer thickness of t = 0.25 μm, effective refractive index of $n_e = 2.0$, and electro-optic coefficient of $r_{33} = 30$ pm/V.

BPM simulations were performed for designing and optimizing the optical components. The directional coupler was designed in two steps. Firstly, in-phase case was designed and the separation between waveguides was calculated to be d = 0.9 μm for full cross-coupling (Fig. 9.7 (d) left). There is a trade-off between the length of the electro-optically defined part of the coupler (i.e. electrode length, Lc) and the applied voltage. For a π phase difference this length is defined as:

$$L_c = \frac{\lambda_0}{2 \times \Delta n(V)} \ . \tag{9.2}$$

In the second stage, the electrode length was scanned from 250 μm to 350 μm with a 50 μm step size while applied voltage value was scanned from 0 to 25 Volts in 1 Volt steps as given in see Fig. 9.7 (c). The most optimum case was obtained for an electrode length of 300 μm and an applied voltage value of 18 Volts to generate a π phase difference. At this voltage level, light will stay in the same arm and be directed to the next MZI section (Fig. 9.7 (d) right).

9.3.3. Ultrahigh-Resolution Spectrometer Layout and Its Working Principle

Fig. 9.8 is the schematic of the ultrahigh-resolution FT spectrometer layout. For ease of understanding the first two levels of the light tapping mechanism are demonstrated. Here a central wavelength of 800 nm is aimed at. There are several MZIs that are electro-optically-controlled in a sequential order. Input light will be divided into two arms with an integrated 3 dB directional coupler. Half of the light will travel through a multi-S-shaped path that is comprised of several curved waveguides and straight waveguide sections. This arm will be used for providing additional length difference between MZI arms. The other half of the light will be sent towards a straight waveguide section that can be considered as the reference arm of the interferometer. The end of the both arms can be a waveguide termination such as a matched load that decreases reflection.
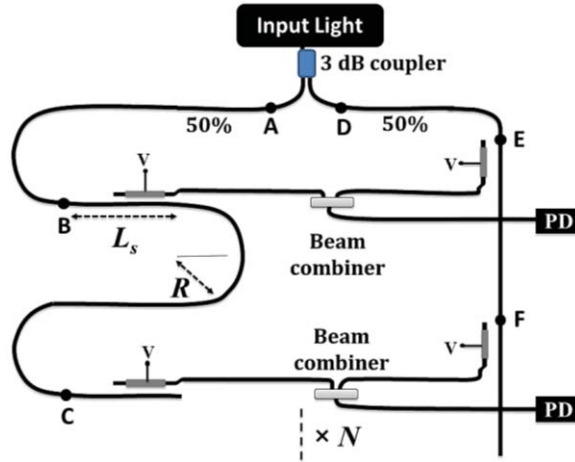
Fig. 9.8. Schematic of the ultrahigh-resolution FT spectrometer design. The input light is divided equally by an on-chip 3 dB coupler and sent towards two different paths; one has several S-shaped waveguides and the other has a straight waveguide. There are several electro-optically-controlled directional couplers on both arms that act as optical switches. They cross-couple the light when there is no voltage, and keep it on the same arm when there is a π phase difference due to electro-optic effect. The cross-coupled light from both arms will be combined at the beam combiner and sent to a photodetector (PD). Here L_s is the length of the straight sections; R is the radius of the curved waveguides on the S-shaped path.

Each MZI consists of two electro-optically-controlled directional couplers one in each arm. The first MZI will have zero path length difference between its arms, therefore the length of segments |AB| and |DE| are equal. The length of the next segment on the multi-S-shaped path is $|BC| = (2 \times \pi \times R) + (2 \times L_s)$ where L_s is the length of the straight parts, and R is the radius of the curved waveguide sections. The length difference between the arms of the next MZI (i.e. |BC| − |EF|) is chosen in accordance with the resolution requirements. The resolution of the spectrometer is defined by the maximum delay $\Delta L_{\max}$, which also determines the spectrometer size. The calculation of $\Delta L_{\max}$ refers to the Littrow condition and can be expressed as [18]:

$$\Delta L_{\max} = \frac{\lambda_0^2}{\delta\lambda \times n_g},\qquad(9.3)$$

where $\delta\lambda$ is the resolution of the spectrometer, n_g is the group refractive index of the waveguide stack, and λ_0 is the center wavelength. For a spectral resolution of 500 MHz a maximum delay of $\Delta L_{\max} \cong 30$ cm is needed which makes it very challenging to accommodate such a spectrometer on a standard 10-inch wafer using existing waveguide SHS designs. The proposed design solves the size problem by using light tapping approach. As the light travels through a waveguide, the optical length gets increased, and by tapping the propagating light out at certain locations on the waveguide, the required optical delay can be obtained for each MZI. The multi-S-shaped sections of this waveguide will keep the length of the device short while straight sections in between (with

length L_s) will mainly provide the optical delay. As a constraint on proper operation of the spectrometer, each MZI path length must be an integer multiple of some fixed path length, i.e. $\Delta L_{max}/N$. The light coming from both MZI arms will get interfered on an on-chip beam combiner and sent to a matched photodetector. The output power distribution digitally processed by using a Fourier transform to retrieve the input spectrum. Photodetectors can be fabricated on the same chip or a commercial photodetector array can be externally butt-coupled to the chip.

Based on the Nyquist sampling theorem, in order to scan 15 GHz of bandwidth with 500 MHz resolution, $N = 60$ directional couplers are needed which results in an overall device size of around 2 cm × 0.5 cm (1 cm^2). The time needed for scanning 15 GHz bandwidth in 60 steps will be less than a millisecond.

9.3.4. Broadband Spectrometer Layout and Its Working Principle

Some applications require high speed spectrometers working over a large bandwidth. The previously explained spectrometer design provides ultrahigh resolution over a very small bandwidth. By changing the spectrometer layout slightly, one can achieve large bandwidth and high speed over a small footprint. Fig. 9.9 demonstrates the FT spectrometer working over 40 nm bandwidth with a spectral resolution of 1 nm at the central wavelength of 800 nm. Such a spectrometer can be used in Raman spectroscopy which can outperform in terms of size and speed compared to existing bulky counterparts. By using Eq. (9.3) the required maximum length difference is calculated to be 372 μm. Assuming 80 MZIs (according to the Nyquist sampling theorem), the required length increment for each step is calculated to be $\Delta L = 4.7$ μm which can be provided by applying a curved waveguide section to one side of the MZI parts.

The working principle of this design is as follows; input light will be divided into two arms with an integrated 3 dB directional coupler. Half of the light will travel through a path that is comprised of several curved waveguides and straight waveguide sections. This arm will be used for providing additional length difference between MZI arms. The other half of the light will be sent towards a straight waveguide section (with small curved sections for avoiding coupling of light between straight sections) that can be considered as the reference arm of the interferometer. The end of the both arms can be a waveguide termination such as a matched load that decreases reflection. In the case of no voltage on the first couplers and a certain voltage (i.e. $V = 18$ Volts) on the rest of the couplers, the light will cross couple to the other branch and stay in the same branch until it reaches the detector. At this stage, there will be no path length difference between two arms. When a certain voltage is applied to the first couplers while there is no voltage on the rest of the couplers, there will be a ΔL path length difference between two arms. By increasing the number of couplers that are under a certain voltage, the path length difference will be increased by ΔL at every step until the maximum path length difference is reached.

The overall device size will be around 2.5 cm × 0.5 cm. The time needed for scanning 40 nm bandwidth in 80 steps will be less than a millisecond.
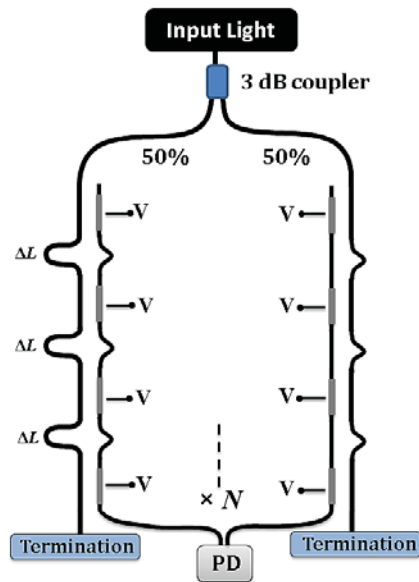
Fig. 9.9. Schematic of the broadband FT spectrometer design. The input light is divided equally by an on-chip 3 dB coupler and sent towards two different paths; one has several curved waveguides and the other has a straight waveguide. There are several electro-optically-controlled directional couplers on both arms that act as optical switches. They cross-couple the light when there is no voltage, and keep it on the same arm when there is a π phase difference due to electro-optic effect. The cross-coupled light from both arms will be interfered at the photodetector (PD). Here ΔL is the extra path length difference between curved and straight waveguide sections.

9.4. Conclusions

In summary, a novel OCT beam scanner, a TD-OCT system and two high-speed FT spectrometer designs were presented to be used in various biomedical optical applications such as OCT, confocal and Brillioun microscopy, and Raman spectroscopy. The proposed designs are comprised of dynamic delay lines which are based on voltage-controlled directional couplers. The proposed ideas can be applied to other imaging modalities as well as other measurement techniques. Different switching mechanisms (e.g. pressure-based) can be applied in different material platforms, depending on the power consumption, and switching speed requirements. It is expected that the layouts described in here will evoke some experimental interest and will be followed up by several research groups and companies.

Acknowledgements

The author thanks Dr. Bob van Someren and Prof. Ton van Leeuwen for the fruitful discussions.

References

[1]. D. Huang, E. A. Swanson, C. P. Lin, J. S. Schuman, W. G. Stinson, W. Chang, M. R. Hee, T. Flotte, K. Gregory, C. A. Puliafito, J. G. Fujimoto, Optical coherence tomography, *Science,* Vol. 254, 1991, pp. 1178-1181.

[2]. B. I. Akca, B. Považay, A. Alex, K. Wörhoff, R. M. de Ridder, W. Drexler, M. Pollnau, Miniature spectrometer and beam splitter for an optical coherence tomography on a silicon chip, *Opt. Express,* Vol. 21, 2013, pp. 16648-16656.

[3]. G. Yurtsever, B. Považay, A. Alex, B. Zabihian, W. Drexler, R. Baets, Photonic integrated Mach-Zehnder interferometer with an on-chip reference arm for optical coherence tomography, *Biomed. Opt. Express*, Vol. 5, 2014, pp. 1050-1061.

[4]. E. L. Wooten, K. M. Kissa, A. Yi-Yan, E. J. Murphy, D. A. Lafaw, P. F. Hallemeier, D. Maack, D. V. Attanasio, D. J. Fritz, G. J. McBrien, D. E. Bossi, A review of lithium niobate modulators for fiber-optic communications systems, *IEEE J. Sel. Top. Quantum Electron.,* Vol. 6, 2000, pp. 69-82.

[5]. O. D. Herrera, K.-J. Kim, R. Voorakaranam, R. Himmelhuber, S. Wang, V. Demir, Q. Zhan, L. Li, R. A. Norwood, R. L. Nelson, J. Luo, A. K.-Y. Jen, N. Peyghambarian, Silica/electro-optic polymer optical modulator with integrated antenna for microwave receiving, *J. Lightwave Technol.*, Vol. 32, Issue 20, 2014, pp. 3861-3867.

[6]. B. I. Akca, C. R. Doerr, G. Sengo, K. Wörhoff, M. Pollnau, R. M. de Ridder, Broad-spectral-range synchronized flat-top arrayed-waveguide grating applied in a 225-channel cascaded spectrometer, *Opt. Express*, Vol. 20, Issue 16, 2012, pp. 18313-18318.

[7]. B. E. Little, T. Murphy, Design rules for maximally flat wavelength-insensitive optical power dividers using Mach-Zehnder structures, *IEEE Photon. Technol. Lett.,* Vol. 9, 1997, pp 1607-1609.

[8]. B. Imran Akca, A. Dana, A. Aydinli, M. Rossetti, L. Li, A. Fiore, N. Dagli, Electro-optic and electro-absorption characterization of InAs quantum dot waveguides, *Opt. Express,* Vol. 16, 2008, pp. 3439-3444.

[9]. N. V. Tkachenko, Optical Spectroscopy, *Elsevier Science*, 2006.

[10]. E. Le Coarer, S. Blaize, P. Benech, I. Stefanon, A. Morand, G. Lerondel, G. Leblond, P. Kern, J. M. Fedeli, P. Royer, Wavelength-scale stationary-wave integrated Fourier-transform spectrometry, *Nat. Photonics,* Vol. 1, 2007, pp. 473-478.

[11]. B. I. Akca, B. Považay, A. Alex, K. Wörhoff, R. M. de Ridder, W. Drexler, M. Pollnau, Miniature spectrometer and beam splitter for an optical coherence tomography on a silicon chip, *Opt. Express*, Vol. 21, Issue 14, 2013, pp. 16648-16656.

[12]. P. Cheben, I. Powell, S. Janz, D.-X. Xu, Wavelength-dispersive device based on a Fourier-transform Michelson-type arrayed waveguide grating, *Opt. Lett.,* Vol. 30, 2005, pp. 1824-1826.

[13]. R. F. Wolffenbuttel, State-of-the-Art in integrated optical microspectrometers, *IEEE Trans. Instrum. Meas.,* Vol. 53, 2004, pp. 197-202.

[14]. M.-L. Junttila, J. Kauppinen, E. Ikonen, Performance limits of stationary Fourier spectrometers, *J. Opt. Soc. Am. A,* Vol. 8, 1991, pp. 1457-1462.

[15]. G. Scarcelli, S. Hyun Yun, Confocal Brillouin microscopy for three-dimensional mechanical imaging, *Nat. Photon.,* Vol. 2, 2008, pp. 39-43.

[16]. J. Harlander, R. J. Reynolds, F. L. Roesler, Spatial heterodyne spectroscopy for the exploration of diffuse interstellar emission lines at far-ultraviolet wavelengths, *Astrophys. J.,* Vol. 396, 1992, pp. 730-740.

[17]. M. Florjańczyk, P. Cheben, S. Janz, A. Scott, B. Solheim, D.-X. Xu, Multiaperture planar waveguide spectrometer formed by arrayed Mach–Zehnder interferometers, *Opt. Express,* Vol. 15, Issue 26, 2007, pp. 18176-18189.

[18]. V. Velasco, P. Cheben, P. J. Bock, A. Delâge, J. H. Schmid, J. Lapointe, S. Janz, M. L. Calvo, D. Xu, M. Florjańczyk, M. Vachon, High-resolution Fourier-transform spectrometer chip with microphotonic silicon spiral waveguides, *Opt. Lett.,* Vol. 38, 2013, pp. 706-708.